Applied Catalysis B: Environmental 125 (2012) 59–66

Contents lists available at SciVerse ScienceDirect

Applied Catalysis B: Environmental

journal homepage: www.elsevier.com/locate/apcatb

WS_2 nanosheets as a highly efficient electrocatalyst for hydrogen evolution reaction

Zhuangzhi Wu[a], Baizeng Fang[b,c], Arman Bonakdarpour[b,c], Aokui Sun[a], David P. Wilkinson[b,c,*], Dezhi Wang[a,**]

[a] Key Laboratory of Ministry of Education for Non-ferrous Materials Science and Engineering, School of Materials Science and Engineering, Central South University, Changsha 410083, China
[b] Department of Chemical & Biological Engineering, University of British Columbia, 2360 East Mall, Vancouver, BC, Canada V6T 1Z3
[c] Clean Energy Research Center, 2360 East Mall, Vancouver, BC, Canada V6T 1Z3

ARTICLE INFO

Article history:
Received 1 March 2012
Received in revised form 8 May 2012
Accepted 11 May 2012
Available online 18 May 2012

Keywords:
Tungsten disulfide
Nanosheets
Preparation
Electrocatalyst
Hydrogen evolution reaction

ABSTRACT

Novel nanostructured material WS_2 nanosheets (NSs) were prepared through a simple and highly reproducible approach, namely, a mechanical activation strategy by using WO_3 and S as the starting materials, and were explored as electrocatalyst for hydrogen evolution reaction (HER). The as-prepared WS_2 NSs reveal separate NSs nanostructure with a sheet thickness of less than 10 nm. On the basis of experimental results obtained under various synthesis conditions, a reasonable reaction process and formation mechanism is proposed, in which the pre-treatment of ball milling is assumed to play a key role for the formation of WS_2 NSs. Due to its large active sites originating from its unique structural characteristics such as loosely stacked layers, providing highly exposed rims particularly edges, WS_2 NSs catalyst has demonstrated high electrocatalytic activity toward HER, which considerably outperforms the commonly used MoS_2 (JDC) catalyst.

1. Introduction

Hydrogen is the most abundant element in the universe and it represents an important alternative energy feedstock, which has been widely pursued as a clean and enabling future energy carrier in the transition from the current hydrocarbon economy.

Particularly, very high energy conversion efficiency can be achieved when hydrogen is combined with fuel cell technology [1]. Therefore, H_2-fueled proton exchange membrane fuel cells exclusively represent the most advanced fuel cell technology [2] and have been of great interest as future energy sources for mobile and stationary applications including zero-emission electric vehicles, distributed home power generators and power sources for small portable electronics [3–8]. Although many important potential applications it still remains a major challenge to produce hydrogen efficiently and inexpensively, and sustainable electrochemical hydrogen production from water splitting has attracted much attention [9–11]. To date, Pt-group metals have been utilized as the most effective electrocatalysts for hydrogen evolution reaction (HER) in an acidic medium [12,13]. However, their low abundance and high cost limit considerably the large scale application of Pt-based catalysts. Recently, great efforts have been made to explore efficient non-noble catalysts [14–18]. Among these catalysts MoS_2 nanoscale materials and amorphous MoS_2 have been extensively investigated [14,19–22]. Although a MoS_2-based catalyst prepared by the deposition of MoS_2 nanoparticles (NPs) on reduced graphene oxide (RGO) has exhibited high catalytic activity toward HER [21], its scale-up application is highly limited at this time because the MoS_2/RGO system is made of MoS_2 synthesized solvothermally and rather expensive RGO [23]. To date, it still remains a big challenge to develop highly efficient less-expensive catalysts for HER.

Due to its structural and electronic similarities to MoS_2, WS_2 has also received intensive investigation as photoelectrochemical catalysts [24–27] and electrocatalysts [28,29]. However, to date only very few paper deals with HER employing WS_2-based materials as electrocatalysts [29]. Interestingly, unpromoted and Co-promoted WS_2 NPs catalysts have demonstrated comparable catalytic activities toward HER compared with their counterparts, unpromoted and Co-promoted MoS_2 catalysts, which reveals a current density of ca. 1.0, 1.5, 5.5 and 4.0 mA/cm^2, respectively, at an overpotential of 300 mV [23,29]. Inspired by this, new nanostructured WS_2 materials with desired morphologies and architectures

* Corresponding author at: Department of Chemical & Biological Engineering, University of British Columbia, 2360 East Mall, Vancouver, BC, Canada V6T 1Z3.
** Corresponding author. Tel.: +86 731 88877221; fax: +86 731 88830202.
E-mail addresses: dwilkinson@chbe.ubc.ca (D.P. Wilkinson), dzwang@mail.csu.edu.cn (D. Wang).

0926-3373/$ – see front matter © 2012 Elsevier B.V. All rights reserved.
http://dx.doi.org/10.1016/j.apcatb.2012.05.013

are expected to improve electrocatalytic activity toward HER. To date, various synthesis approaches have been investigated to produce WS_2 with diversified morphologies and structures, which include high-temperature sulfurization [30], magnetron sputtering [31], thermal decomposition [32–34], laser ablation [35], chemical vapor deposition [36–39], sonochemical synthesis and hydrothermal/solvothermal route [40–42]. Recently, developments of 2D nanosheets (NSs) crystals such as stable graphene and transition-metal chalcogenides have sparked new discoveries in condensed-matter physics and electronics [43]. Further miniaturization of these 2D structures by lateral confinements can potentially bring not only the modulation of electron-transport phenomena but also the enhancement of their 2D host capabilities which arise from the enlarged surface area and improved diffusion processes upon the intercalation of guest molecules. Cheon et al. attempted to prepare 2D WS_2 NSs with the assistance of surfactant molecules by rolling out of 1D tungsten oxide nanorods [44]. Gedanken et al. attempted to fabricate WS_2 nanoplates through carving phenomena, but the final nanoplates stacked too densely, resulting in a low exposed surface area [45]. Tang et al. prepared hexagonal WS_2 nanoflakes by adopting tungsten oxide nanorods as precursors [46]. Although so, it still remains a major challenge to synthesize 2D WS_2 by a simple and reproducible and scalable approach, because WS_2 has a layer structure similar to graphite and prefers to form densely stacked bulk microplates or closed nanostructures such as quasi-0D onion-like structures or nanotubes (NTs) to decrease the number of dangling bonds and the total energy of the system [44,47–49].

In this paper, separate 2D WS_2 NSs have been produced through a simple and reproducible mechanical activation strategy, i.e., ball-milling, a proven powerful approach to produce nanostructured metal sulfides [50,51] followed by annealing at elevated temperatures, by using WO_3 and S as the starting materials. The as-prepared WS_2 NSs reveal separate nanostructure with a sheet thickness of less than 10 nm. To our knowledge, this is the first report of the solid-state synthesis of separate WS_2 NSs obtained by the exfoliation of sulfide layers of primary WO_3 particles. On the basis of the evolution of the structure and morphology with reaction conditions, a possible reaction process and formation mechanism for WS_2 NSs has been elucidated. Due to its fantastic nanostructural characteristics such as loosely stacked layers which provides highly exposed rims and edges, WS_2 NSs catalyst has revealed a high electrocatalytic activity toward HER, which outperforms greatly the commonly used nanoscaled MoS_2 catalyst from JDC (Jinduicheng Molybdenum Group, China).

2. Experimental

2.1. Synthesis of WS_2 NSs

In a typical synthesis, 5 g of WO_3 and 10 g of S were mixed and energetically ball-milled in a planetary ball mill with 900 g of stainless balls as milling media at 400 rotations per minute (rpm) for 24 h in an atmosphere of argon. Then, 1 g of the ball-milled mixture and 5 g of sulfur were loaded into two individual boats and quickly pushed into the hot zone of the tube furnace which has been heated up to 600 °C under argon, and the mixture and sulfur were placed in the middle and upstream side of the tube, respectively. The furnace was kept at this temperature for 2 h and then cooled to room temperature. After that, black WS_2 powder was collected.

2.2. Preparation of catalyst electrode

For determination of activity toward HER for various catalysts, a three-electrode electrochemical cell (i.e., half-cell) was employed, and linear sweep voltammetry (LSV) measurements were conducted at room temperature in 0.5 M H_2SO_4 with a scan rate of 2 mV/s using saturated calomel electrode (SCE) as the reference electrode and Pt foil as the counter electrode. Electrolyte solution was deaerated by high-purity nitrogen for 1 h prior to any LSV measurement. The working electrode was a thin layer of Nafion-impregnated catalyst cast on a glassy carbon disk of 3 mm diameter embedded in a Teflon cylinder. The catalyst layer was fabricated as follows: 4 mg of catalyst and 80 μL of 5 wt% Nafion solution were dispersed in 1 mL of a solution of deionized water and ethanol (4:1 in volume ratio). After stirring by ultrasonication for 1 h, 5 μL of catalyst slurry was pipetted and spread on the top of a glassy carbon disk. The catalyst-coated glassy carbon electrode was dried at 80 °C for 2 h to yield a catalyst loading of 285 $\mu g\,cm^{-2}$.

2.3. Characterization

The as-obtained products were analyzed by scanning electron microscopy (SEM) on a FEI Sirion 200 microscope. Transmission electron microscopy (TEM) images and selected-area electron diffraction (SAED) patterns were obtained using a Tecnai G^2 20 transmission electron microscopy operating at 200 keV equipped with a double tilt sample holder. High resolution TEM (HRTEM) analysis and fast Fourier transforms (FFT) were carried out on a JEOL 2010F transmission electron microscopy. Specimens for TEM and HRTEM investigations were prepared by sonicating in alcohol followed by placing a drop of the solution on a carbon-film-coated holey copper grid. X-ray diffraction (XRD) patterns were recorded using Cu Kα radiation on a D/max-2500 diffractometer. N_2 adsorption and desorption isotherms were measured at 77 K on a KICT SPA-3000 Gas Adsorption Analyzer after a sample was degassed at 423 K to 20 mTorr for 12 h. The specific surface areas were determined from nitrogen adsorption using the Brunauer–Emmett–Teller (BET) method.

Electrocatalytic activity toward HER was conducted in the three-electrode electrochemical cell mentioned above. Electrode potentials were recorded vs SCE reference electrode, which was calibrated with respect to reversible hydrogen electrode (RHE). The calibration was performed in the high purity H_2 saturated electrolyte with a Pt wire as the working electrode as reported by Li et al. [21]. All the potentials reported here are referred to RHE according to $E\,(\mathrm{RHE}) = E\,(\mathrm{SCE}) + 0.273\,\mathrm{V}$ [21].

3. Results and discussion

3.1. Surface and structural characteristics of WS_2 NSs

Various nanostructured WS_2 materials have been prepared through ball-milling the starting materials WO_3 and S followed by a heat treatment at various temperatures. A typical XRD pattern for the WS_2 NSs sample prepared at 600 °C for 2 h is shown in Fig. 1, which reveals a high purity of WS_2 for the as-obtained sample. All the reflections can be indexed to the pure hexagonal WS_2 (JCPDS card No. 08-0237). The calculated distance between two lattice planes ($c/2$) is about 0.621 nm, which is larger than that of WS_2 (platelets of 2H arrangement, 0.618 nm) distinctly. There is a little lattice expansion of about 0.5%, which may be attributed to the introduction of strain owing to curvature of the layers [30].

SEM images with different magnifications of the WS_2 NSs are shown in Fig. 2. As revealed in Fig. 2(a), all the NSs are separate, which are different from the previously reported WS_2 nanoplates with close stacking [45]. Individual NSs are typically between hundreds of nanometers and several micrometers in size. From the higher magnification images shown in Fig. 2(b)–(d), more detailed morphologies of the NSs are observed. It is evident that the

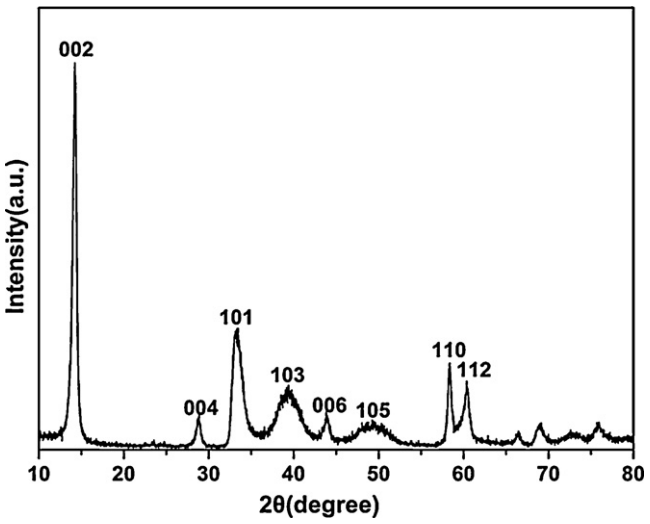

Fig. 1. XRD pattern for the WS_2 NSs obtained at 600 °C for 2 h.

thickness of the individual WS_2 NSs is only ca. 10 nm. In addition, it is also observed that small fraction of WS_2 NSs roll up to form nanoflowers with helical twisted petals, as shown in Fig. 2(e) and (f). Generally, in the absence of external forces, the individual 2D NSs prefer to roll up to form closed structures in order to decrease the number of dangling bonds and the total energy of the system.

Further insight into the morphology and structure of the NSs can be obtained through their TEM and HRTEM images as shown in Fig. 3. In Fig. 3(a), one can see that the WS_2 NSs are stacked loosely, and a portion of them are slightly curved. The SAED pattern taken on an individual NS reveals a well-indexed pure hexagonal structure of 2H-WS_2. Just as reported [36,44,49], the 2D NSs are unstable and tend to form closed structures by rolling up. Therefore, a portion of WS_2 NSs also form NTs by rolling up as shown in Fig. 3(b), which is a transition state of rolling process and a half-tube and half-sheet structure is developed. Moreover, a complete WS_2 NT is also depicted as shown in the inset to reveal the rolling process. Fig. 3(c) reveals that individual NSs have a thickness of only ca. 5 nm, indicating that WS_2 NSs are stacked loosely by less than 10 monolayers. The HRTEM image and the corresponding FFT pattern shown in Fig. 3(d) indicate that the WS_2 NSs are well crystallized with clearly observable lattice fringes and uniform planar base plane.

To get a better understanding of the formation mechanism of WS_2 NSs, the conditions for the synthesis were studied systematically in a series of experiments. In all these experiments only one parameter was changed at a time. To investigate the influence of temperature, various temperatures such as 500 °C, 600 °C, 700 °C,

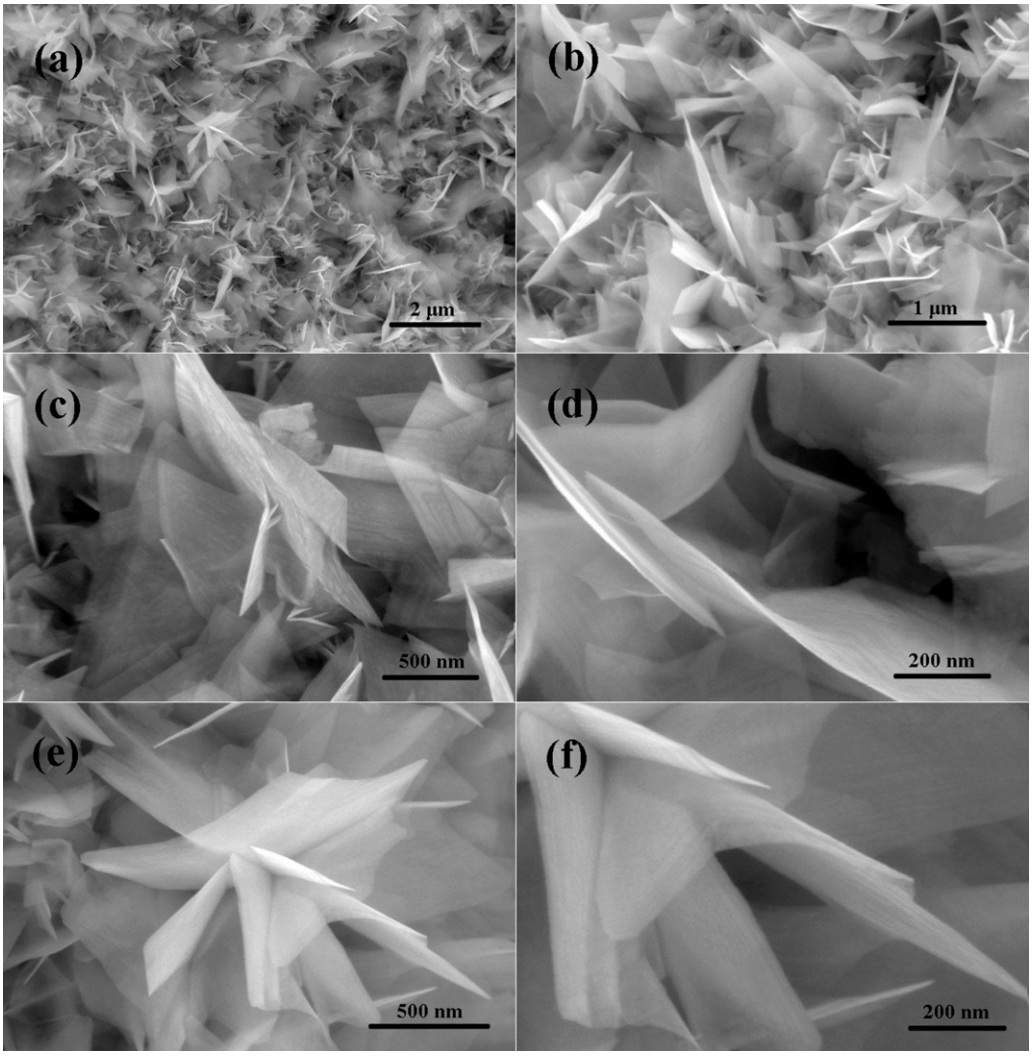

Fig. 2. SEM images with various magnifications for the WS_2 NSs obtained at 600 °C for 2 h.

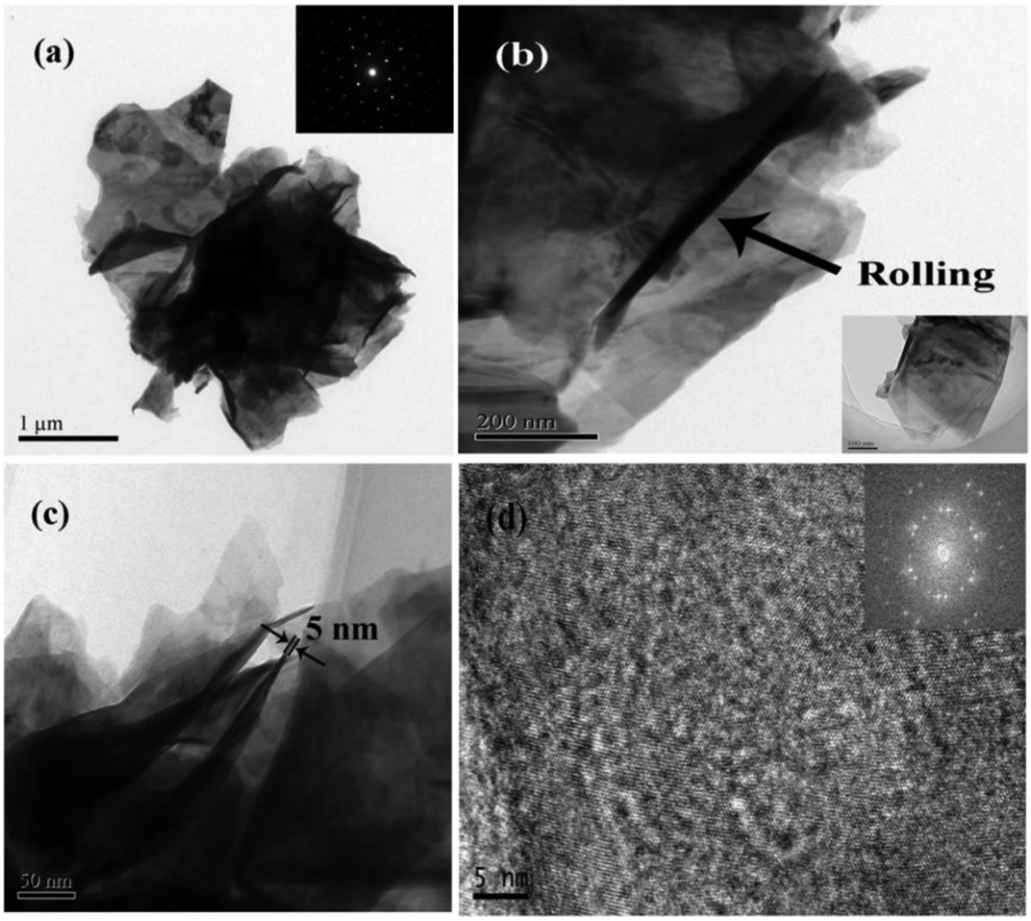

Fig. 3. TEM images for the WS_2 NSs obtained at 600 °C for 2 h: (a) low-magnification image and SEAD pattern of an individual NS (inset); (b) images for rolling NSs and a formed NT (inset); (c) image for single NSs and (d) HRTEM image for a single NS and its corresponding FFT (inset).

800 °C and 840 °C were applied for the synthesis of WS_2 NSs [51]. It was found that pure WS_2 NSs could only be obtained at 600 °C and 700 °C. At a lower temperature (i.e., 500 °C), the reaction rate was so slow that only a little WS_2 nanoplates were obtained and most of the WO_3 still kept the primary quasi-spherical structure, as shown in Fig. S1(a). A possible formation mechanism may be proposed according to the coexistence of the inner WO_3 quasi-spheres and exterior WS_2, in which the WS_2 nanoplates are produced by the exfoliation of the outer sulfide layers. When the reaction temperature is increased up to 840 °C, the reaction rate is accelerated, but there are still no pure WS_2 NSs obtained. This is because the evaporation of sulfur is also accelerated at this temperature, resulting in the lack of enough sulfur for the complete sulfurization of WO_3 under the same condition. The as-prepared WS_2 are hexagonal nanoflakes, as shown in Fig. S1(b), similar to that reported by Li et al. [46], due to the intrinsic symmetry of corresponding lattices. Moreover, Yang et al. [52] reported that inorganic fullerene-like (IF)-WS_2 could be synthesized at 500–650 °C for 30 min in their synthetic route, adopting S and WO_3 as reactants in an atmosphere of H_2, and higher temperatures or longer reaction times would result in 2H-WS_2. Particularly, they claimed that almost all products were transformed into 2H-WS_2 at 800 °C. However, surprisingly, in the present case, IF-WS_2 can be obtained only at a temperature higher than 800 °C and WS_2 NSs can only be prepared at lower temperatures (i.e., 600–700 °C). As revealed by the TEM images shown in Fig. S2, these IF-WS_2 are much huger than those in the previous report (about 50 nm) [52], and the diameter is even larger than the theoretically maximal value of 200 nm [53,54], as marked by an arrow. But many particles with large sizes are not completely sulfurized because of the fast evaporation of S and the slow diffusion process of sulfurization, resulting in dark cores (unreacted WO_3) as evident in Fig. S2(d). Generally, it was thought that no fullerene structures could be obtained from the oxide nanoparticles in the absence of H_2 [54]. However, herein, IF-WS_2 particles are actually obtained through the direct reaction between WO_3 and S without hydrogen, which should be attributed to the quickly formed WS_2 shell during high-temperature annealing. After ball milling together for 24 h, WO_3 particles are totally covered by S and they form a stable WS_2 shell after high-temperature annealing to limit the size and shape of the final particles. Then a diffusion process of S is followed to sulfurize the inner oxide core to produce IF-WS_2 according to the classical "*outside-in*" mechanism [53–55]. Moreover, if the outermost layers are not stable, they will break into pieces in the form of NSs, which also can be observed in Fig. S2(a).

The samples annealed at 600 °C for different times were examined by XRD and FE-SEM. The XRD pattern shown in Fig. S3 reveals that when the reaction time is 10 min, the sulfurization is not completed with the coexistence of WS_2 and WO_3 without any other intermediate oxides. However, when the reaction time is increased more than 30 min, pure WS_2 can be obtained. Yang et al. reported that the WO_3 could be sulfurized completely at 620 °C for only 10 min [52]. While, in our case, more reaction time is required. This abnormal phenomenon can be attributed to the size effect with the assistance of H_2, because the WO_3 nanoparticles they adopted were less than 100 nm and the sulfurization was conducted in an atmosphere of H_2. To investigate the growth process of WS_2 NSs, the transition states of sulfurization were captured when the reaction

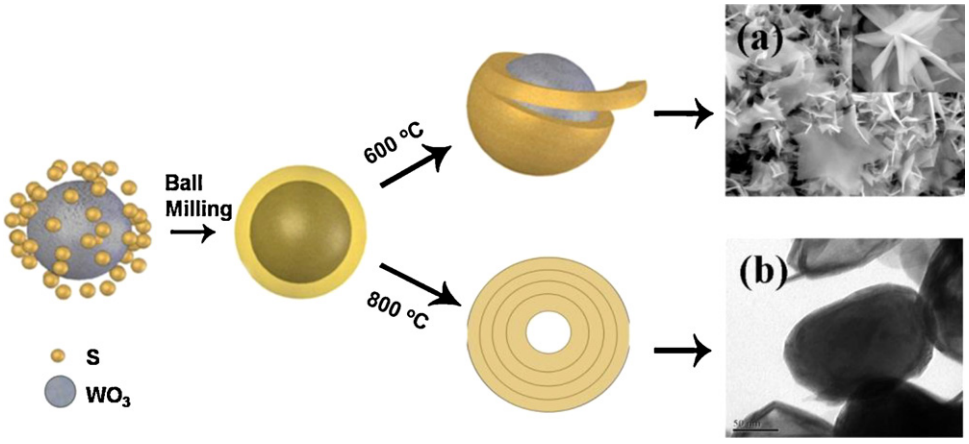

Fig. 4. Schematic illustration for the formation processes of WS_2 NSs (a) and fullerene nanostructures (b).

time was 10 min and 20 min, respectively. As revealed by the SEM images for transition stages in Fig. S4, flake-like WS_2 and quasi-spherical WO_3 coexist with a reaction time of 10 min (Fig. S4(a)). Interestingly, these WS_2 nanoflakes are exfoliated from the outer sulfide layers of WO_3 with curved shape, as marked by arrows (Fig. S4(b)), corresponding to Fig. 4(a). With the increasing of reaction time (i.e., 20 min), more quasi-spherical WO_3 particles are converted into flake-like WS_2, and even tubular and helical NSs are also observed because of rolling up, which preserve a similar structure to the inset of Fig. 3(b), as shown in Fig. S4(c) and (d). Upon up to 30 min, the conversion is finished and pure WS_2 NSs with a yield of 100% can be obtained (Fig. S3(b)).

We consider that the pretreatment of ball milling plays an important role in the formation process of WS_2 NSs. Therefore, comparative studies were also carried out. The mixture of WO_3 and S without ball milling was also annealed at 600 °C for 2 h under the same condition. From the SEM images shown in Fig. S5(a), it is obvious that only small portion of the quasi-spherical WO_3 particles are sulfurized into lamellar WS_2 structures, and most of them are transformed into suboxides WO_x (x = 2–3), such as $W_{10}O_{29}$ and WO_2, which can be identified by the XRD pattern shown in Fig. S5(b). However, even if the WO_3 was ball-milled and then mixed with sulfur, perfect WS_2 NSs still cannot be obtained and the impurity such as Fe is involved in the formats of $FeWO_4$ and Fe_2WO_6, as shown in Fig. S5(c) with XRD pattern shown in Fig. S5(d). Evidently, the only difference is that the S in the mixture is not ball-milled with WO_3 together to get close contact. Therefore, it is considered that the ball milling not only plays a crucial role in the activation but also in the homogeneous distribution of reactants to facilitate fast and complete sulfurization. Moreover, the excess S can also prevent WO_3 from reacting with the impurity of Fe. In a typical sulfurization process, the S in the ball-milled mixture is not enough to support the whole process due to the fast evaporation, and most of the reaction is finished by the following S vapor from upstream boats. However, comparing Fig. S5(c) with Fig. 2, it can be concluded that S in the mixture plays a special role in the formation of separate WS_2 NSs, not only preventing the involvement of impurity but also inducing and directing the growth of separate NSs. A possible formation process will be accordingly prospected later.

Generally, the WS_2 nanostructures are prepared by the sulfurization of oxide powder in a reducing atmosphere (H_2S or its mixture with H_2 and N_2) [52–55], and the reaction processes are stepwise, including a reduction and a subsequent sulfurization step. In a typical reaction process, primary WO_3 is firstly reduced into suboxide WO_x, and then sulfurized into final WS_2. Many intermediate suboxides can be detected, such as WO_2, $W_{18}O_{49}$ and $W_{20}O_{58}$. But there are not any intermediate suboxides detected in the present reaction, indicating that the reaction herein is a fast and direct one, resulting in the production of WS_2 directly. The chemical reaction is simply described as follows:

$$2WO_3 + 7S = 2WS_2 + 3SO_2$$

This abnormal phenomenon can be attributed to the activation effect of ball milling, which lowers the reaction temperature and accelerates the reaction rate to get a direct sulfurization. Typically, in the presence of H_2 at high temperatures, the first step of reduction from trioxide to suboxide is very quick and the sulfurization takes place only after reduction of the oxide nanoparticles, and this situation further slows the rate of sulfur/oxide exchange since much higher energy would be required for sulfur to break the stronger oxygen-metal bond of sub- or dioxide as compared with this bond in trioxide [54]. In the present work, the action of H_2 in the previous reports can be replaced by S, and the direct sulfurization of WO_3 is easier than that of suboxide or dioxide. Therefore, after being activated by ball milling, the present reaction is faster than the previous reports [53,54] under similar conditions, and no intermediates can be detected. Otherwise, the intermediates of WO_x will be found without ball-milling pretreatment, as indicated by the XRD pattern in Fig. S5(b).

Based on the above results and discussions a possible reaction process and formation mechanism for WS_2 NSs is proposed. Firstly, a homogeneous distribution of S on WO_3 can be realized through ball-milling WO_3 and S microparticles for a long time (i.e., 24 h), and the hard WO_3 cores are always covered by excess S. Then, at the first instant of the reaction, WS_2 shells are produced in the interface during the annealing. At a high temperature (i.e., 800 °C), these shells are stable enough to limit the size and shape of the inner oxide, and IF-WS_2 can be obtained through "*outside-in*" mechanism by diffusion of S. For microparticles with large sizes, the sulfurization process will require more reaction time and WS_2/WO_3 shell/core structures will be produced. However, at a low temperature (i.e., 600–700 °C), because of its lower growth rate the sulfide layer on the surface of the large oxide particle is not sufficient to wrap the entire surface, and it breaks up into small pieces. Layer by layer, WS_2 NSs can be produced in a high yield through the exfoliation of outer sulfide layers. However, it must be noted that the mechanical activation before the annealing plays a crucial role in the formation of WS_2 NSs. The ball milling is believed to break WO_3 particles into small pieces in order to create large quantity of WO_3 sites for S intimately coating the surface. During the annealing, WS_2 shell is produced and then peeled off to form NSs. After the outer layer (i.e., WS_2 shell) peels away, WO_3 particles become smaller and more active than the ones with larger size, and it becomes

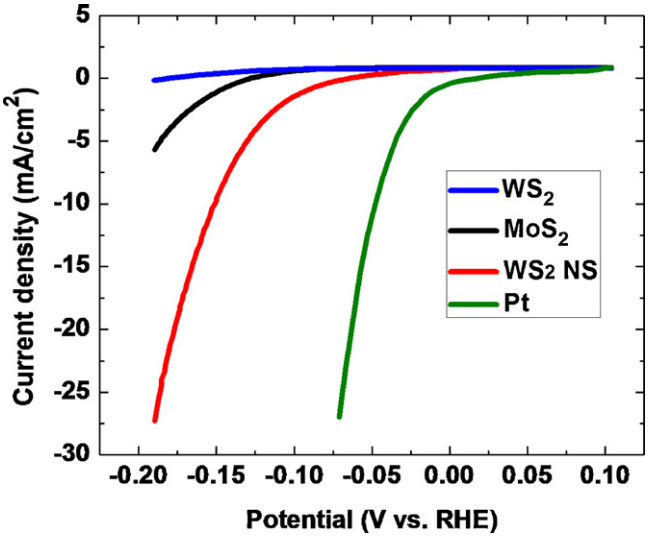

Fig. 5. Polarization performance curves obtained in 0.5 M H_2SO_4 for various electrocatalysts.

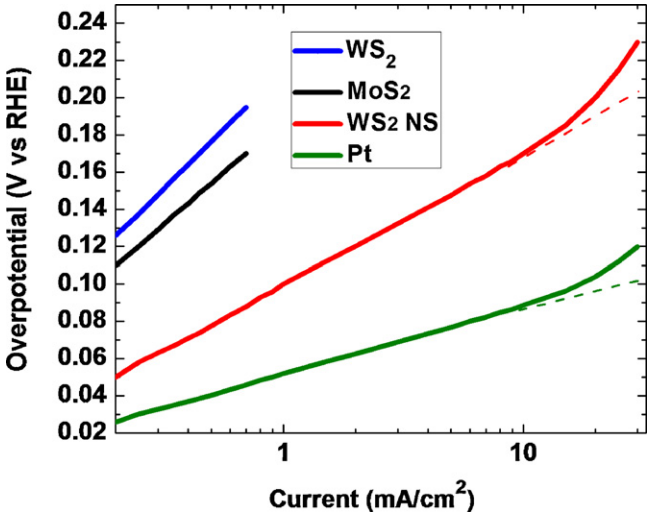

Fig. 6. Tafel plots derived for various electrocatalysts.

easier for S to coat their outer surface to form new WS_2 shell. This process is expected to last until all WO_3 particles are used. As for the WO_3 and S particles without mechanical activation of ball milling, due to large particle size of WO_3 and S particles and particularly their loosely contact the sulfurization is conducted in a slow and stepwise way with intermediate products of WO_x, resulting in incomplete sulfurization and densely stacked structures, which are evident in the SEM image shown in Fig. S5(a), and the XRD pattern shown in Fig. S5(b). Moreover, it should also be emphasized that the initial WS_2 shell in the interface can act as a template to induce and direct the growth of WS_2 NSs. If there is no WS_2 shell in the interface, thin NSs will be produced in many local domains and no huge and perfect separate NSs can be obtained, as shown in Fig. S5(c). A typical schematic illustration for the formation processes of WS_2 NSs and fullerene nanostructures is depicted in Fig. 4. Tailored from top and expanded around the internal core at 600 °C, the exfoliated sulfide layers will form single NSs or tubular twisted helix (the inset), as shown in Fig. 4(a). While, when the core is wrapped by stable sulfide layers at 800 °C, fullerene nanostructures will be obtained (Fig. 4(b)).

3.2. Electrocatalytic activity toward HER

As a typical application, WS_2 NS was explored as an electrocatalyst for HER. For comparison, a commercially available MoS_2 (JDC) catalyst, commercial carbon black (Vulcan XC-72R) supported Pt(20 wt%) (E-TEK) and the WS_2 sample obtained without the ball-milling pretreatment, were also investigated for this application. Fig. 5 presents their corresponding polarization curves measured in 0.5 M H_2SO_4 with a scan rate of 2 mV/s at room temperature. Pt exhibits high HER activity with a near zero overpotential. An overpotential of ca. −100 mV (vs RHE) beyond which the cathodic current rise rapidly under more negative potentials was observed for MoS_2 electrode while a significantly lower overpotential (ca. −60 mV vs RHE) was observed for WS_2 NSs electrode. Interestingly, the WS_2 sample obtained without the ball-milling pretreatment shows a little higher overpotential (ca. −120 mV vs RHE) than the MoS_2 electrode. It is worthwhile to note that a large difference in the electrocatalytic activity toward HER can also be observed. At an overpotential of −150 mV, a current density of ca. 9.66 mA/cm^2 was observed, which is much higher than that observed for MoS_2 (ca. 1.12 mA/cm^2) electrode, suggesting the electrocatalytic activity of WS_2 NSs electrode is ca. 8.6 times that achieved by MoS_2. The higher electrocatalytic activity of WS_2 NSs may be attributable to its larger active sites, resulting from its unique structural characteristics such as separate NSs with loosely stacked layers, providing highly exposed rims particularly edges which afford abundant accessible catalytic sites for the HER and to adsorb H. In contrast, the commercially available MoS_2 sample reveals large-sized (ca. several micrometers) plates with densely stacked layers, as shown in Fig. S6. Evidently, the MoS_2 sample can only afford much smaller active sites for the HER due to much less exposed rims and edges.

The Tafel plots derived from Fig. 5 are shown in Fig. 6 where their linear portions were fit to the Tafel equation ($\eta = b \log j + a$, where j is the current density and b is the Tafel slope) to determine Tafel slopes. The Tafel plots reveal a slope of ca. 33 mV/dec for commercial Pt(20 wt%)/VC, which is very close to that observed by Li et al. [21]. They also show slopes of ca. 115 mV/dec for commercially available MoS_2 and 138 mV/dec for the WS_2 sample obtained without ball-milling, which are basically agreement with that reported for transition metal sulfides by other researchers (i.e., 120 and 135 mV/dec for nano-particulate MoS_2 and WS_2, respectively) [29], suggesting that the current could be transport limited [29]. Interestingly, a smaller Tafel slope of ca. 72 mV/dec was observed for the WS_2 NSs catalyst, which is much smaller than that (i.e., 138 mV/dec) observed for the WS_2 sample obtained without ball-milling and even significantly smaller than that (i.e., 115 mV/dec) observed for the commercially available MoS_2. For practical applications, smaller Tafel slope is favorable because faster increase in HER rate with the increasing overpotentials can be expected [23].

In addition to Tafel slope, another inherent measure of activity for the HER is the exchange current density (j_0) [56], which is determined by fitting $i - E$ data to the Tafel equation. MoS_2 (JDC) reveals a j_0 of 1.7×10^{-7} A/cm^2, which is comparable to that of nanoparticulate MoS_2 reported by Jaramillo et al. [14], while the WS_2 sample obtained without the ball-milling pretreatment shows a remarkably lower j_0 (0.2×10^{-7} A/cm^2). Interestingly, the WS_2 NSs catalyst demonstrates a j_0 of 2.5×10^{-6} A/cm^2, which is much higher than that observed for the WS_2 sample obtained without the ball-milling pretreatment and also higher than that of MoS_2 (JDC).

Although WS_2 NSs catalyst demonstrates better performance than the commercial MoS_2 (JDC) catalyst, it does not mean that the WS_2 NSs catalyst is the best non-precious HER catalyst. In fact, lots of research reports have claimed that WS_2 is inferior to MoS_2 in electrocatalytic activity toward HER if they have same or similar nanostructures. For instance, density functional theory (DFT) calculations suggest hydrogen evolution on MoS_2 is expected to take

Table 1
BET surface areas and catalytic activities toward HER for various metal sulfides.

Sample	S_{BET} (m^2/g)	j_0 (A/cm^2)	Normalized j_0 (A/$cm^2{}_{BET}$)
WS_2 NTs	10.2	2.5×10^{-6}	8.5×10^{-8}
WS_2	1.6	0.2×10^{-7}	0.44×10^{-8}
MoS_2 (JDC)	3.7	1.7×10^{-7}	1.6×10^{-8}

place predominantly at the Mo-edge (hydrogen binding energies $\Delta G_H = 0.08$ eV) rather than the S-edge ($\Delta G_H = 0.18$ eV), while for WS_2 both edges are equally good ($\Delta G_H = 0.22$ eV) [29]. Given these values for ΔG_H, non-promoted MoS_2 is predicted to be a better hydrogen evolution catalyst than WS_2.

Compared with other metal sulfides counterparts higher electrocatalytic activity observed for WS_2 NSs is probably attributable to its larger surface area (N_2 adsorption isotherms measurements shown in Fig. S7 reveal a BET surface area of 10.2 m^2/g for the WS_2 NSs, 3.7 m^2/g for the JDC MoS_2 and 1.6 m^2/g for the WS_2 sample obtained without ball-milling pretreatment) particularly much more exposed edge sites. To have a better insight into the relationship between the catalytic activity toward HER and BET surface area for various metal sulfide catalysts, the data including BET surface areas, j_0, and j_0 values normalized by the BET surface areas are summarized and shown in Table 1. It is evident that both j_0 and normalized j_0 values increase with increasing BET surface areas, however, the increase in normalized j_0 values is not linear, namely, although BET surface area of WS_2 NSs is about 2.76 times that of MoS_2 (JDC), the normalized j_0 value observed for WS_2 NSs is about 5.3 times of the latter. When compared with the WS_2 sample obtained without ball-milling pretreatment, the enhancement in normalized j_0 value observed for WS_2 NSs is about 19 times although the increase in BET surface area is ca. 6.4 times. These observations suggest that BET surface area of a catalyst is not a dominant factor in determining catalytic activity toward HER. High catalytic activity observed for WS_2 NSs may mainly results from its highly exposed edges.

Because the structure of WS_2 is similar to that of MoS_2, which reveals that sulfided $\bar{1}\,0\,1\,0$ Mo-edge is the active site for H_2 evolution [14,20] and hydrodesulfurization (HDS) [59], it is expected for WS_2 NSs to exhibit similar crystal plane-dependent catalytic activity for HER, namely, the basal plane is inert and active sites are supposed to be located on edge planes of WS_2.

From the TEM analysis it can be concluded that most of the exposed huge planes of WS_2 NSs are inert basal planes rather than active edge planes. Therefore, although the HER activity for WS_2 NSs is about 8–10 times that of MoS_2 (JDC), the HER activity of WS_2 NSs may be further promoted if the ratio of basal/edge planes can be reduced, which deserves further study. Interesting, Jaramillo et al. claimed that controlled sintering allows one to change the ratio of basal plane sites to edge sites without changing the nature of the MoS_2 edge [14]. In addition, different rims on edge planes may affect the HER activity of electrocatalyst, just like the similar phenomena observed in HDS. Thus, it should be very interesting to clarify the functions of the top and bottom rim planes, and that of the edge sites in the separate WS_2 NSs and closely-stacked NS structures.

Inspired by high catalytic activity toward HER demonstrated by WS_2 NSs, and also the successful preparation of MoS_2 NSs in our previous work [57], we were planning to investigate MoS_2 NSs for its catalytic activity toward HER, and expecting further improvement in HER activity from this material.

High durability and cycling performance is another important measure for a good electrocatalyst. For the assessment of this parameter, the WS_2 NS catalyst electrode was cycled continuously for 1000 cycles. Fig. 7(a) shows the polarization plots at the end of cycling and 1st one (i.e., initial), from which it is evident the

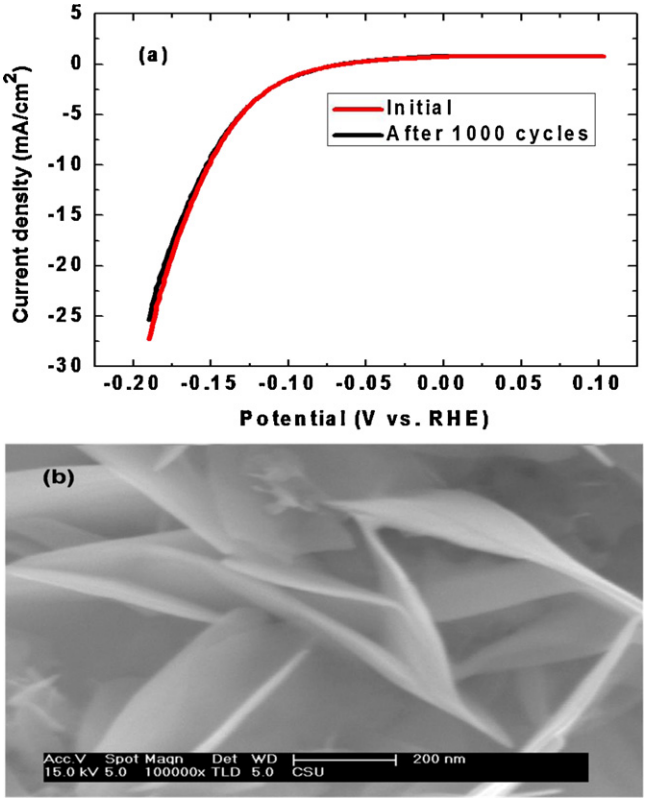

Fig. 7. Polarization performance curves obtained in the initial and after 1000 cycles (a) and SEM image after 1000 cycles (b) for the WS_2 NS catalyst.

novel WS_2 NS electrocatalyst reveals a similar *I–V* curve after 1000 cycles to the first one with negligible loss in the cathodic current, suggesting excellent durability and cycling performance for this material. The high durability observed for WS_2 NSs is probably mainly attributed to that the cycling test time is not too long and the electrolyte is not too acidic. Interestingly, a similar observation about electrochemical stability of nanostructured MoS_2 in 0.5 M H_2SO_4 has recently been reported by Chen et al. [58]. They claimed that no degradation in electrochemical activity was observed from potential cycling up to 10,000 cycles, which is longer than that reported in our study. The SEM image after 1000 cycles shown in Fig. 7(b) reveals that WS_2 NSs retain their morphology without any visible degradation, suggesting good stability for WS_2 NSs electrocatalyst.

From the results reported in this study it is found that the WS_2 nanosheets catalyst not only has high catalytic activity toward HER but also good durability and cycling performance, which suggests it is stable enough in the operating condition. Contamination from sulfur and/or its compounds produced by the decomposition of WS_2 nanosheets is supposed to be negligible. Although so, further study on its stability especially at the high current densities in which PEM electrolyzers are operated may examine any possible cavitation damage to the NSs caused by H_2 bubbles, and further investigation along this direction will help one understand better about electrocatalysts for HER and/or fuel cells and develop more stable, efficient and less expensive catalysts. To further explore the long term stability of WS_2 NSs in the future, chemical analysis of the sample before and after long term stability tests will be conducted. Some other techniques such as energy-dispersive X-ray spectroscopy, X-ray photoelectron spectroscopy or auger electron spectroscopy will be employed to look at changes in the atomic ratio of sulfur to tungsten before and after tests. If some sulfur were

converted to H_2S, then one would expect to see the ratio of (S/W) to decrease especially at the surface.

Generally, WS_2 nanosized catalysts were reported to have smaller catalytic activity toward HER than MoS_2 ones [29]. Interestingly, in our study it was found that WS_2 NS reveals a much higher catalytic activity than the commercial MoS_2 catalyst. In addition, the catalytic activity toward HER can be greatly improved by using graphene as support or Co as doping agent. Thus, further improvement in catalytic toward HER may be expected if WS_2 NS is combined with graphene or doped by Co. Research work along this direction is in progress.

4. Conclusions

In conclusion, a simple and efficient strategy, by ball-milling the starting materials WO_3 and S followed by annealing at 600–700 °C, has been developed to fabricate elegant separate WS_2 NSs. The as-obtained WS_2 NSs are only several nanometers in thickness, and a few of them tend to roll up to form tube-like or helical twisted nanostructures owing to increased peripheral dangling bonds. The mechanical activation is found to play a crucial role in the formation process of the separate WS_2 NSs, resulting in a rapid and direct sulfurization without any intermediates. The reaction process and formation mechanism are proposed on the basis of experimental facts. Moreover, IF-WS_2 is also produced by the present method at a higher temperature (i.e., 800 °C), only adopting WO_3 and S as reactants in the absence of H_2. This synthesis strategy provides a promising approach for the large-scale fabrication of separate WS_2 NSs. Due to its fantastic structural characteristics such as separate NSs with loosely stacked layers which provide highly exposed edges as active catalytic sites, the WS_2 NSs catalyst has demonstrated high electrocatalytic activity toward HER, which outperforms considerably its counterparts, commercially available MoS_2 and the WS_2 obtained without the ball-milling pretreatment electrocatalysts.

Acknowledgments

This work was supported by the National High Technology Research and Development Program of China (863 program) (2007AA06Z129), Hunan Provincial Innovation Foundation for Postgraduate (CX2010B041) and Scholarship Award for Excellent Doctoral Student granted by Ministry of Education of China.

Appendix A. Supplementary data

Supplementary data associated with this article can be found, in the online version, at http://dx.doi.org/10.1016/j.apcatb.2012.05.013.

References

[1] R. Borup, J. Meyers, B. Pivovar, Y.-S. Kim, R. Mukundan, N. Garland, D. Myers, M. Wilson, F. Garzon, D. Wood, Chemical Reviews 107 (2007) 3904–3951.
[2] N. Tian, Z.-Y. Zhou, S.-G. Sun, Y. Ding, Z.-L. Wang, Science 316 (2007) 732–735.
[3] B.-Z. Fang, N.-K. Chaudhari, M.-S. Kim, J.-H. Kim, J.-S. Yu, Journal of the American Chemical Society 131 (2009) 15330–15338.
[4] B.-Z. Fang, J.-H. Kim, M.-S. Kim, J.-S. Yu, Chemistry of Materials 21 (2009) 789–796.
[5] B.-Z. Fang, J.-H. Kim, M.-S. Kim, M.-W. Kim, J.-S. Yu, Physical Chemistry Chemical Physics 11 (2009) 1380–1387.
[6] B.-Z. Fang, M.-S. Kim, J.-H. Kim, M.-Y. Song, Y.-J. Wang, H.-J. Wang, D.P. Wilkinson, J.-S. Yu, Journal of Materials Chemistry 21 (2011) 8066–8073.
[7] J.-L. Qiao, B. Li, D.-J. Yang, J.-X. Ma, Applied Catalysis B: Environmental 91 (2009) 198–203.
[8] H.A. Gasteiger, S.S. Kocha, B. Sompalli, F.T. Wagner, Applied Catalysis B: Environmental 56 (2005) 9–35.
[9] M.S. Dresselhaus, I.L. Thomas, Nature 414 (2001) 332–337.
[10] M.G. Walter, E.L. Warren, J.R. McKone, S.W. Boettcher, Q. Mi, E.A. Santori, N.S. Lewis, Chemical Reviews 110 (2010) 6446–6473.
[11] J.K. Lee, Y.M. Yi, H.J. Lee, S.H. Uhm, J.Y. Lee, Catalysis Today 146 (2009) 188–191.
[12] D.E. Bartak, B. Kazee, K. Shimazu, T. Kuwana, Analytical Chemistry 58 (1986) 2756–2761.
[13] P. Millet, F. Andolfatto, R. Durand, International Journal of Hydrogen Energy 21 (1996) 87–93.
[14] T.F. Jaramillo, K.P. Jorgensen, J. Bonde, J.H. Nielsen, S. Horch, I. Chorkendorff, Science 317 (2007) 100–102.
[15] A. Le Goff, V. Artero, B. Jousselme, P.D. Tran, N. Guillet, R. Metaye, A. Fihri, S. Palacin, M. Fontecave, Science 326 (2009) 1384–1387.
[16] X.L. Hu, B.S. Brunschwig, J.C. Peters, Journal of the American Chemical Society 129 (2007) 8988–8998.
[17] B. Winther-Jensen, K. Fraser, C. Ong, M. Forsyth, D.R. MacFarlane, Advanced Materials 22 (2010) 1727–1731.
[18] F. Harnisch, G. Sievers, U. Schröder, Applied Catalysis B: Environmental 89 (2009) 455–458.
[19] P.D. Tran, A. Le Goff, J. Heidkamp, B. Jousselme, N. Guillet, S. Palacin, H. Dau, M. Fontecave, V. Artero, Angewandte Chemie International Edition 50 (2011) 1371–1374.
[20] B. Hinnemann, P.G. Moses, J. Bonde, K.P. Jorgensen, J.H. Nielsen, S. Horch, I. Chorkendorff, J.K. Norskov, Journal of the American Chemical Society 127 (2005) 5308–5309.
[21] Y.-G. Li, H.-L. Wang, L.-M. Xie, Y.-Y. Liang, G.-S. Hong, H.-J. Dai, Journal of the American Chemical Society 133 (2011) 7296–7299.
[22] D. Merki, S. Fierro, H. Vrubel, X.-L. Hu, Chemical Science 2 (2011) 1262–1267.
[23] D. Merki, X.-L. Hu, Energy & Environmental Science 4 (2011) 3878–3888.
[24] A. Sobczynski, A. Yildiz, A.J. Bard, A. Campion, M.A. Fox, T. Mallouk, S.E. Webber, J.M. White, Journal of Physical Chemistry 92 (1988) 2311–2315.
[25] A. Sobczynski, Journal of Catalysis 131 (1991) 156–166.
[26] A. Di Paola, L. Palmisano, M. Derrigo, V. Augugliaro, Journal of Physical Chemistry B 101 (1997) 876–883.
[27] W. Ho, J. Yu, J. Lin, J.-G. Yu, P. Li, Langmuir 20 (2004) 5865–5869.
[28] C.M.B. Holt, S. Murphy, M.R. Gray, D. Mitlin, Catalysis Communications 12 (2010) 314–317.
[29] J. Bonde, P.G. Moses, T.F. Jaramillo, J.K. Nørskovb, I. Chorkendorff, Faraday Discussions 140 (2008) 219–231.
[30] R. Tenne, L. Margulis, M. Genut, G. Hodes, Nature 360 (1992) 444–446.
[31] K. Ellmer, Physica Status Solidi 245 (2008) 1745–1760.
[32] C.M. Zelenski, P.K. Dorhout, Journal of the American Chemical Society 120 (1998) 734–742.
[33] S. Bastide, D. Duphil, J.P. Borra, C. Levy-Clement, Advanced Materials 18 (2006) 106–109.
[34] Y.-D. Li, X.-L. Li, R.-R. He, J. Zhu, Z.-X. Deng, Journal of the American Chemical Society 124 (2002) 1411–1416.
[35] J.-J. Hu, J.S. Zabinski, J.H. Sanders, J.E. Bultman, A.A. Voevodin, Journal of Physical Chemistry B 110 (2006) 8914–8916.
[36] X.-L. Li, J.-P. Ge, Y.-D. Li, Chemistry: A European Journal 10 (2004) 6163–6171.
[37] A. Margolin, F.L. Deepak, R. Popovitz-Biro, M. Bar-Sadan, Y. Feldman, R. Tenne, Nanotechnology 19 (2008) 095601.
[38] N. Zink, J. Pansiot, J. Kieffer, H.A. Therese, M. Panthofer, F. Rocker, U. Kolb, W. Tremel, Chemistry of Materials 19 (2007) 6391–6400.
[39] N. Zink, H.A. Therese, J. Pansiot, A. Yella, F. Banhart, W. Tremel, Chemistry of Materials 20 (2008) 65–71.
[40] N.A. Dhas, K.S. Suslick, Journal of the American Chemical Society 127 (2005) 2368–2369.
[41] H.A. Therese, J.-X. Li, U. Kolb, W. Tremel, Solid State Sciences 7 (2005) 67–72.
[42] J.F. Wu, X. Fu, Materials Letters 61 (2007) 4332–4335.
[43] A.K. Geim, K.S. Novoselov, Nature Materials 6 (2007) 183–191.
[44] J.-W. Seo, Y.-W. Jun, S.-W. Park, H. Nah, T. Moon, B. Park, J.-G. Kim, Y.-J. Kim, J. Cheon, Angewandte Chemie International Edition 46 (2007) 8828–8831.
[45] V.-G. Pol, S.-V. Pol, A. Gedanken, Crystal Growth and Design 8 (2008) 1126–1132.
[46] P.-G. Li, M. Lei, X.-F. Wang, H.-L. Tang, W.-H. Tang, Journal of Alloys and Compounds 474 (2009) 463–467.
[47] R. Tenne, Nature Nanotechnology 1 (2006) 103–111.
[48] A. Vojvodic, B. Hinnemann, J.K. Norskov, Physical Review B 80 (2009) 125416.
[49] A. Yella, E. Mugnaioli, M. Panthofer, U. Kolb, W. Tremel, Angewandte Chemie International Edition 49 (2010) 3301–3305.
[50] Z.-Z. Wu, D.-Z. Wang, A.-K. Sun, Journal of Crystal Growth 312 (2010) 340–343.
[51] Z.-Z. Wu, D.-Z. Wang, X.-Q. Zan, A.-K. Sun, Materials Letters 64 (2010) 856–858.
[52] H.-B. Yang, S.-K. Liu, J.-X. Li, M.-H. Li, G. Peng, G.-T. Zou, Nanotechnology 17 (2006) 1512.
[53] Y. Feldman, G.L. Frey, M. Homyonfer, V. Lyakhovitskaya, L. Margulis, H. Cohen, G. Hodes, J.L. Hutchison, R. Tenne, Journal of the American Chemical Society 118 (1996) 5362–5367.
[54] Y. Feldman, V. Lyakhovitskaya, R. Tenne, Journal of the American Chemical Society 120 (1998) 4176–4183.
[55] R. Tenne, M. Homyonfer, Y. Feldman, Chemistry of Materials 10 (1998) 1556–1562.
[56] B.E. Conway, B.V. Tilak, Electrochimica Acta 47 (2002) 3571–3594.
[57] Z.-Z. Wu, D.-Z. Wang, Y. Wang, A.-K. Sun, Advanced Engineering Materials 12 (2010) 534–538.
[58] Z.-B. Chen, D. Cummins, B.N. Reinecke, E. Clark, M.K. Sunkara, T.F. Jaramillo, Nano Letters 11 (2011) 4168–4417.
[59] M. Daage, R.R. Chianelli, Journal of Catalysis 149 (1994) 414–427.